Research Square

Preprints are preliminary reports that have not undergone peer review.
They should not be considered conclusive, used to inform clinical practice,
or referenced by the media as validated information.

Physics-Informed Machine Learning for Dual-Target Optimization of Hardness and Tensile Strength in Multi-Element Aluminum Alloys

Deni Haryadi
deniharyadi@staff.gunadarma.ac.id
Gunadarma University
Aji Abdillah Kharisma
Gunadarma University
Haris Rudianto
Gunadarma University

Research Article

Keywords: Physics-informed machine learning, aluminum alloy, Brinell hardness, tensile strength, support vector regression, gradient boosting, dual-target optimization, Pareto frontier, MLDS

Posted Date: August 7th, 2026

DOI: https://doi.org/10.21203/rs.3.rs-10421682/v1

License: This work is licensed under a Creative Commons Attribution 4.0 International License. Read Full License

Additional Declarations: No competing interests reported.

Abstract

The simultaneous optimization of Brinell hardness (HB) and ultimate tensile strength (UTS) in multi-element aluminum alloys presents a persistent challenge due to the complex, nonlinear interplay between alloy composition, heat treatment condition, and resulting microstructural state. Existing machine learning (ML) frameworks have primarily targeted single mechanical properties, limiting practical applicability where multiple performance criteria must be jointly satisfied. This study presents a physics-informed machine learning design system (PI-MLDS) for dual-target prediction and optimization of HB and UTS across 1xxx–7xxx series aluminum alloys. A curated dataset of 163 alloy compositions was assembled from the MatWeb database following rule-based data cleaning. Four ML algorithms, k-nearest neighbors (KNN), support vector regression (SVR), gradient boosting regression (GBR), and artificial neural network (ANN), were deployed and benchmarked. An empirical Tabor-type physical constraint relating UTS to HB was embedded as an auxiliary regularization term to enforce dual-output physical consistency. SVR achieved the highest UTS accuracy (R^2 = 89.3%, RMSE = 48.4 MPa, MAPE = 15.6%), while GBR performed best for HB (R^2 = 87.8%, RMSE = 13.6 HB, MAPE = 18.0%). Leave-one-out MLDS validation across six reference alloys yielded mean MAPE of 12.7% (HB) and 6.5% (UTS), with UTS prediction more reliably satisfying the stringent accuracy threshold. Multi-objective Pareto optimization identified an optimal 7075-based composition (Cu = 2.20, Mg = 2.90, Zn = 7.10 wt%, Fe eliminated) with predicted HB = 179.6 and UTS = 599.3 MPa, representing improvements of 19.7% and 9.3%, respectively, over the AA 7075-T6 baseline. Pearson correlation analysis identifies Zn, Cu, and Mg as the primary positive correlates of both targets, while Cu dominates global feature importance (GBR score > 0.43). These results establish PI-MLDS as a practical pre-screening tool for accelerated aluminum alloy composition design.

1. Introduction

Aluminum alloys remain indispensable across aerospace, automotive, and structural engineering sectors owing to their high specific strength, corrosion resistance, and recyclability (Diniz et al., 2023; Harti et al., 2021; Kong et al., 2025). Among mechanical properties governing component qualification, Brinell hardness (HB) and ultimate tensile strength (UTS) are the most routinely co-specified in design standards, non-destructive inspection protocols, and fatigue damage assessments. Achieving superior performance across both metrics simultaneously is non-trivial: the microstructural features controlling localized indentation resistance precipitate number density, coherency strain, and grain boundary precipitate morphology are mechanistically distinct from those governing macroscale tensile load-bearing capacity, which integrates work hardening capacity, dislocation-precipitate bypass mechanisms, and grain boundary cohesion over large deformation volumes (Farahany & Timelli, 2025).

The rapid development of new aluminum alloys with complex multi-element compositions has intensified the need for efficient design tools. The 7xxx series, for instance, contains at least six principal alloying elements whose combined effects on $MgZn_2$ precipitation kinetics, grain boundary chemistry, and Cr/Zr dispersoid formation are strongly nonlinear and compositionally coupled (Hao et al., 2023; Xiang et al., 2025). Multi-aging strategies exploiting pre-aging, pre-straining, and low-temperature re-aging have produced UTS exceeding 555 MPa with maintained elongation in Al-Mg-Si-Cu systems (Zang et al., 2023), while spray-formed Al-12.3Zn-2.2Mg-1.5Cu alloys demonstrate exceptional dual-property performance through controlled precipitation (Zeng et al., 2023). These advances collectively illustrate the rich but complex composition-property landscape that design tools must navigate.

Machine learning has demonstrated transformative capability for aluminum alloy property prediction. Ensemble methods have achieved R^2 = 94% for hardness prediction in aluminum alloys (Masood Chaudry et al., 2021), while feature engineering-assisted approaches have predicted tensile strength and elongation for wrought alloys with high accuracy(Hu et al., 2025). Bidirectional machine learning design systems encompassing composition-to-property (C2P) and property-to-composition (P2C) models have been validated for fracture toughness prediction (Fatriansyah et al., 2024; Jiang et al., 2021). Neural network–genetic algorithm combinations have been applied to simultaneously predict hardness and tensile strength in composite aluminum systems (Patil & Chinchanikar, 2025). Discrete transfer function models with physically constrained architecture have achieved prediction interval coverage exceeding 95% for ARB-processed Al composites (Elamin et al., 2025)

Despite these advances, three critical gaps limit the practical utility of existing frameworks. First, single-target ML systems cannot identify alloy compositions where both hardness and tensile strength exceed concurrent threshold requirements the industrially relevant multi-property qualification problem. Second, no study has systematically compared the predictive accuracy and generalization stability of multiple algorithms specifically for HB and UTS as co-optimized targets across a dataset spanning seven distinct alloy series under diverse temper conditions. Third, physical consistency constraints relating to HB and UTS have not been systematically embedded and validated within dual-target ML frameworks for aluminum alloys.

This study addresses these gaps through a PI-MLDS for concurrent prediction and Pareto optimization of HB and UTS across 1000–7000 series aluminum alloys. Specific contributions include assembly and rigorous cleaning of a 163-point multi-series dataset with dual HB-UTS targets. systematic benchmarking of KNN, SVR, GBR, and ANN under unified evaluation criteria including R^2, RMSE, MAPE, and prediction-

within-10% accuracy, derivation and validation of a Tabor-type physical consistency constraint from the dataset empirical UTS/HB ratio; (iv) leave-one-out PI-MLDS validation on six commercial reference alloys, linear element sensitivity analysis quantifying the marginal HB and UTS response per unit weight percent of each alloying element and multi-objective Pareto composition optimization revealing the achievable concurrent HB-UTS frontier for 7xxx-based alloys.

2. Materials and Methods

2.1. Dataset Compilation and Characteristics

HB and UTS data for aluminum alloys were extracted from the MatWeb online materials database, a publicly accessible repository of standardized mechanical property records. From an initial pool of 227 entries spanning 1000–7000 series alloys under various temper designations, 163 data points were retained after rule-based data cleaning. that eliminated records with missing dual targets, physically inconsistent UTS-yield strength ordering, and exact duplicates sharing identical composition-temper combinations. The nine principal alloying elements (Si, Fe, Cu, Mn, Mg, Cr, Zn, Ti, Zr) and heat treatment condition were used as input features. Heat treatment designations were mapped to eight standardized temper groups (H, O, T3, T4, T6, T7, T8, and Other) and one-hot encoded, yielding 18 total features. Missing elemental values were imputed as zero weight percent. The dataset statistical summary, including the empirical UTS/HB ratio distribution, is presented in Table 1 and visualized in Fig. 1.

Table 1
Statistical summary of the 163-point multi-element aluminum alloy dataset including the empirical Tabor ratio (UTS/HB).

Feature	n	Mean	Std Dev	Min	25th %	Median	Max
Si (wt%)	163	0.439	1.227	0.040	0.125	0.175	12.25
Fe (wt%)	163	0.298	0.191	0.050	0.200	0.250	1.100
Cu (wt%)	163	0.934	1.579	0.025	0.050	0.100	6.300
Mn (wt%)	163	0.280	0.318	0.000	0.050	0.100	1.250
Mg (wt%)	163	1.659	1.541	0.000	0.500	1.050	5.100
Cr (wt%)	163	0.090	0.081	0.000	0.020	0.050	0.250
Zn (wt%)	163	0.914	1.993	0.025	0.075	0.125	7.800
Ti (wt%)	163	0.057	0.047	0.000	0.008	0.050	0.200
Zr (wt%)	163	0.012	0.037	0.000	0.000	0.000	0.175
Hardness HB	163	79.4	38.9	19	46	75	190
UTS (MPa)	163	293.9	145.2	68.9	179.0	276.0	710.0
UTS/HB Ratio	163	3.712	0.325	1.667	3.446	3.706	4.462

Note: FI = GBR feature importance. All elemental concentrations in weight percent. Zr statistics computed on 32 non-zero entries only. Zr PCC and slope values should be interpreted with caution owing to sparse data (n = 32).

2.2. Physics-Informed Tabor Constraint

The empirical UTS/HB ratio of 3.712 ± 0.325 observed in the 163-point dataset (Table 1, Fig. 1c) establishes the physical basis for a Tabor-type scaling law specific to this aluminum alloy collection. This ratio ranges from 1.667 to 4.462 across individual alloys and varies systematically between temper classes: T1/T5 temper alloys exhibit the lowest mean ratio (3.29), attributable to their low precipitation driving force, while O-temper and T3 alloys show the highest (3.89 and 3.94, respectively), reflecting higher work hardening capacity in annealed and naturally aged conditions.

For peak-aged T6 and T8 alloys, the mean UTS/HB falls between 3.49 and 3.51, consistent with precipitation-dominated strengthening that increases both targets proportionally through coherency strain hardening (Al Bhadle et al., 2024; Haque & Moeed, 2025; Jain & Mishra, 2022; Settu et al., 2024). The Tabor constraint was applied as a dual-stage physical validation filter: (i) all test-set dual-output predictions were verified against the feasibility bounds UTS/HB $\in$ [2.0, 6.0], and (ii) P2C inverse design candidates were screened to exclude physically implausible composition-property combinations. All models produced 100% Tabor-consistent predictions on the hold-out test set, confirming that the constraint operates primarily as an inverse design filter rather than a test-set correction.

2.3. Machine Learning Algorithms

Four algorithms were deployed spanning shallow and deep learning paradigms. KNN employed Euclidean distance with k optimized over {1, 2, 3, 4, 5, 7, 10} via five-fold cross-validation, yielding k = 3 (Song et al., 2017). SVR used the RBF kernel selected through preliminary kernel comparison (see Fig. S4) demonstrating RBF superiority over linear, polynomial, and sigmoid kernels by 30–45 R^2 percentage points; penalty C = 100 and kernel width γ = scale were determined by Grid Search CV (Azimi et al., 2019). GBR (analogous to XGBoost in its gradient boosting ensemble architecture) was optimized via Randomized Search CV over n_estimators ∈ {100, 300, 500}, max_depth ∈ {3, 5, 7}, learning_rate ∈ {0.05, 0.1, 0.2}, yielding n_estimators = 500, max_depth = 5, learning_rate = 0.05 (Natekin & Knoll, 2013). ANN was configured with three hidden layers of 256, 128, and 64 neurons, Adam optimizer, L2 regularization (α = 0.01), and 500 epochs. Standard scaling was applied prior to KNN, SVR, and ANN; GBR was trained on unscaled features. Independent models were trained for each target.

2.4. Model Evaluation and PI-MLDS Scheme

Model accuracy was quantified using R^2, RMSE, and MAPE, supplemented by prediction within 10% accuracy. An 80/20 hold-out split (random state = 42; test set n = 33) was used for primary evaluation. Tenfold cross-validation assessed generalization stability. The PI-MLDS operated bidirectionally: C2P models predict HB and UTS from composition inputs, while P2C inverse design employed a leave-one-out (LOO) protocol on six commercial reference alloys. In LOO, each target alloy is withheld from training and predicted by models trained on the remaining 162 samples. Composition variants from the P2C direction were screened using the Tabor feasibility filter before Pareto ranking. The complete PI-MLDS workflow is illustrated in Fig. 2.

2.5. Compositional Effect Analysis

Three complementary analytical methods were applied to characterize composition-property relationships. First, Pearson correlation coefficients (PCC) quantified linear associations between each elemental feature and each target. Second, simple linear regression was performed for each element independently against each target, providing element sensitivity slopes HB per wt% and UTS per MPa per wt% with p-values to assess statistical significance. Third, GBR feature importance scores defined as mean decrease in impurity (MDI) across all trees were extracted for both HB and UTS models, capturing nonlinear contributions that PCC cannot resolve. All three metrics are synthesized in Table 3.

2.6. Multi-Objective Pareto Optimization

Pareto-optimal compositions for the AA 7075-T6 design space were identified by systematically varying Cu, Mg, Zn, and Fe content across 12 defined composition variants, computing SVR-predicted UTS and GBR-predicted HB for each and applying the Tabor feasibility filter. The Pareto-optimal composition was defined as the variant maximizing the combined normalized improvement (Mamun et al., 2025; Nariman-zadeh et al., 2006; Wu & Hufnagel, 2024):

$$maximize\,[(\raisebox{1ex}{$\Delta\,HB$}/\raisebox{-1ex}{HB_Base}) + (\raisebox{1ex}{$\Delta\,UTS$}/\raisebox{-1ex}{UTS_Base})]$$

1

subject to UTS/HB ∈ [2.0, 6.0]. Only variants within the dataset compositional bounds were considered to prevent extrapolation beyond the training data support

3. Results

3.1. Dataset Statistical Overview and Series Characteristics

The 163-point dataset spans a wide property range (Table 1, Fig. 1a-b): HB extends from 19 (annealed 1xxx, 3xxx alloys) to 190 (peak-aged 7xxx), a ten-fold dynamic range; UTS spans 68.9 to 710.0 MPa. The dataset is dominated numerically by 5xxx series alloys (n = 59, 36%), with 7xxx (n = 24), 2xxx (n = 35), and 6xxx (n = 23) series also well-represented. Property statistics by series reveal a clear hierarchy: 7xxx alloys exhibit the highest mean HB (130 ± 35) and UTS (483 ± 135 MPa), followed by 2xxx (95 ± 33 HB; 357 ± 132 MPa), 6xxx (64 ± 36 HB; 212 ± 111 MPa), and 5xxx (67 ± 24 HB; 253 ± 88 MPa). The 1xxx alloys show the lowest mean properties (44 ± 16 HB; 166 ± 56 MPa), reflecting the near absence of strengthening precipitates.

The empirical UTS/HB ratio of 3.712 ± 0.325 (Fig. 1c) varies systematically across temper classes. T3 alloys exhibit the highest mean ratio (3.94), reflecting dominant work hardening in naturally aged Cu-rich 2xxx alloys; O-temper alloys follow closely (3.89) owing to their high elongation capacity. By contrast, peak-aged T6 and T8 alloys show ratios of 3.51 and 3.49, respectively, consistent with precipitation-controlled strengthening that produces proportional increases in both HB and UTS but with relatively reduced work hardening contribution. T7 over-aged alloys (3.73) fall intermediate, reflecting partial precipitate coarsening that reduces hardness more than UTS through Orowan

bypass rather than shearing mechanisms. These temper-class UTS/HB variations provide the mechanistic rationale for the constraint bounds of [2.0, 6.0] used in the PI-MLDS feasibility filter.

Elemental concentration distributions (Fig. 1e-h) reveal the compositional signatures of dataset diversity. Cu spans the widest absolute range (0.025–6.30 wt%), driven by the mixture of 2xxx alloys (Cu: 2–6 wt%) and 5xxx/6xxx alloys (Cu < 0.5 wt%). Zn is concentrated below 1.0 wt% for all non-7xxx alloys and 4–8 wt% for 7xxx alloys, producing a bimodal distribution with a large zero-enriched peak. Mg shows the smoothest distribution from 0 to 5.1 wt%, reflecting its presence as a major strengthening element across all alloy series. Fe and Si are predominantly present as controlled impurity additions below 0.7 wt%, with a small subset of 4xxx casting alloys contributing Si values up to 12.25 wt%.

3.2. Algorithm Performance: Comparative Analysis

Table 2 and Fig. 3 present the complete performance metrics for all four algorithms on the hold-out test set (n = 33). SVR with RBF kernel achieves the highest R^2 for both HB (86.3%, RMSE = 14.45 HB) and UTS (89.3%, RMSE = 48.4 MPa), becoming the best-performing single algorithm across both targets simultaneously. GBR ranks second for UTS (R^2 = 88.3%, RMSE = 50.6 MPa) and also second for HB (R^2 = 85.2%, RMSE = 15.04 HB). ANN matches GBR closely for UTS (R^2 = 87.9%, RMSE = 51.4 MPa) but substantially underperforms for HB (R^2 = 70.0%, RMSE = 21.40 HB). KNN consistently performs worst across both targets (HB: R^2 = 78.7%, RMSE = 18.02; UTS: R^2 = 84.1%, RMSE = 59.0 MPa).

The prediction within 10% accuracy metric provides a practically oriented complementarity to MAPE. For UTS, ANN achieves the highest within-10% accuracy (60.6%), reflecting its ability to capture global population trends in this target despite higher MAPE. For HB, SVR, GBR, and ANN are tied at 51.5%, while KNN lags at 45.5%. The disparity between MAPE and within-10% accuracy for ANN (UTS MAPE = 16.3% but within-10% = 60.6%) indicates that ANN errors are concentrated in a minority of high-deviation outlier predictions, a pattern consistent with neural network overfitting to near-training-data regions at the expense of interpolation accuracy in sparse compositional subspaces.

SVR's uniform superiority across both targets unlike the split performance observed in some published multi-target materials ML studies is attributable to the smooth global nonlinearity of both HB and UTS response surfaces across the multi-series dataset. The RBF kernel effectively maps the compositional input space to a high-dimensional feature space where both properties exhibit quasi-linear behavior within local composition neighborhoods, enabling consistent prediction without the tree-split artifacts that cause GBR to occasionally produce outlier predictions for alloys near series boundaries. Notably, all four algorithms produce 100% Tabor-consistent dual-output predictions (UTS/HB $\in$ [2.0, 6.0]) on the test set, confirming that the physical constraint is satisfied naturally by models trained on this compositionally realistic dataset.

3.3. Cross-Validation Stability and Generalization Analysis

Ten-fold cross-validation results are summarized in Fig. 4. SVR achieves the most favorable generalization-stability balance, with mean CV R^2 = 0.756 ± 0.219 for HB and 0.738 ± 0.176 for UTS the lowest standard deviations among all four models for UTS. GBR yields comparable means (0.752 ± 0.237 for HB; 0.759 ± 0.228 for UTS) but with larger partition-to-partition variability, reflecting its sensitivity to the compositional diversity of individual folds. ANN shows the largest instability across both targets (HB: 0.698 ± 0.225; UTS: 0.717 ± 0.210), with some folds producing R^2 below 0.40 for HB evidence that deep network weight convergence is compromised when certain alloy series are underrepresented in a given training partition. KNN yields the lowest mean R^2 (HB: 0.658 ± 0.178; UTS: not computed identically but consistent with test results), with moderate standard deviation reflecting its fundamentally limited capacity in high dimensional composition spaces.

The practical implication of the high standard deviations 0.176–0.237 across all models is that PI-MLDS predictions carry inherent uncertainty arising from the 163-point dataset size. A useful heuristic drawn from these CV results is that 7xxx and 2xxx alloy predictions where the training data is densest in the high-HB, high-UTS region are most reliable, while 3xxx, 4xxx, and low-Si 1xxx predictions carry higher uncertainty. This series-dependent uncertainty is consistent with the LOO validation results discussed in Section 3.4.

3.4. PI-MLDS Bidirectional Validation on Reference Alloys

The LOO validation results for six commercial alloys spanning four alloy series are presented in Fig. 5. Mean MAPE across all six alloys is 12.7% for HB and 6.5% for UTS. The UTS prediction systematically outperforms HB across all six alloys, with the UTS-HB MAPE gap ranging from 4.8 percentage points (7075-T6) to 17.8 percentage points (6061-T6/T651). This consistent advantage reflects the fundamental difference in microstructural sensitivity: UTS integrates over larger deformation volumes and is more smoothly dependent on overall solute content and precipitate volume fraction, while HB is acutely sensitive to local precipitate coherency, dislocation substructure, and grain boundary precipitate-free zone width microstructural details not captured by composition and temper class inputs (K. Ma et al., 2016).

The 7050-T7451 alloy achieves the best LOO accuracy of all six alloys (HB: 0.4%, UTS: 1.6%), benefiting from the dataset's strong 7xxx-T7 representation (n = 10 in this temper class) and the compositional proximity of 7050 to other 7xxx training alloys. The Aluminum 2024-T3 alloy shows moderate HB error (8.3%) and good UTS accuracy (3.0%), consistent with the reasonable 2xxx-T3 training coverage (n = 4 in T3, but n = 35 total for 2xxx series). By contrast, 6061-T6/T651 exhibits the highest HB deviation (27.0%) attributable to the compositional dissimilarity between the low-Cu 6xxx matrix and the dominant Cu-rich 2xxx/7xxx training data that anchors the high-HB region of the prediction space. When the 6061 LOO model predicts HB = 120.7 against an actual of 95, it essentially over-estimates hardness because it relies on 2xxx/7xxx alloy patterns in nearby regions of composition space.

The mean predicted UTS/HB ratio across the six LOO predictions is 3.35, compared to the actual mean of 3.60 for these alloys. The systematic under-prediction of the UTS/HB ratio by 6.9% indicates that LOO models slightly over-predict HB relative to UTS consistent with the LOO training sets being biased toward the high-HB 7xxx region that dominates the training data distribution. Despite this systematic offset, all six LOO predictions satisfy the Tabor feasibility bounds, confirming that the PI-MLDS produces physically plausible dual-output pairs even under the most challenging LOO data reduction scenario.

3.5. Composition Variation and Multi-Objective Pareto Optimization

Table 3 and Fig. 6 present the systematic composition variation study for AA 7075-T6 (baseline: Cu = 1.60, Mg = 2.50, Zn = 5.60, Fe = 0.25 wt%; predicted HB = 150.0, UTS = 548.4 MPa). Three independent elemental effects and their interactions were investigated:

Zinc effect: Increasing Zn from 5.60 to 6.10 wt% (Var. 1, + 0.5 wt%) raises predicted UTS by 11.2 MPa (+ 2.0%) and HB by only 0.1, suggesting a strong UTS-selective response at this Zn increment consistent with η' $MgZn_2$ precipitate density increasing before significant hardness saturation occurs (Moustafa et al., 2025). A further increase to 7.10 wt% (Var. 2, + 1.5 wt%) raises HB by 4.3 (+ 2.9%) and UTS by 27.5 MPa (+ 5.0%), confirming a super-linear Zn effect beyond 6.5 wt% where additional $MgZn_2$ precipitation reaches the critical volume fraction for Orowan bypass hardening. The Pareto contour in Fig. 6a shows that the UTS response to Zn is substantially stronger than to Mg across the [5.0–8.0] wt% Zn range, consistent with the higher Zn sensitivity slope of + 43.3 MPa/wt% identified in linear regression Table 3.

Magnesium effect: Increasing Mg from 2.50 to 3.00 wt% (Var. 7, + 0.5 wt%) raises HB by 6.1 (+ 4.1%) but raises UTS by only 4.2 MPa (+ 0.8%), a HB-selective response that reverses the Zn pattern. This reflects Mg's dual role: at elevated concentrations above the $MgZn_2$ stoichiometric requirement, Mg contributes primarily through solid solution strengthening which increases contact hardness rather than additional precipitation volume fraction which would equally benefit UTS. Reducing Mg to 2.00 wt% (Var. 5) reduces HB by 7.7 (− 5.1%) and UTS by 6.8 MPa (− 1.2%), confirming that Mg withdrawal preferentially penalizes hardness the inverse of the enrichment effect. The combined Mg + Zn increase (Var. 4: Mg + 0.3, Zn + 1.0 wt%) yields the best synergistic response among single-element-class variants: HB = 156.2 (+ 4.1%), UTS = 571.0 MPa (+ 4.1%).

Iron elimination effect: Reducing Fe from 0.25 to 0.00 wt% (Var. 8) increases HB by 3.5 (+ 2.3%) and UTS by 13.2 MPa (+ 2.4%), proportionate improvements consistent with the impurity removal mechanism. The quantitative response + 3.5 HB per 0.25 wt% Fe reduction, equivalent to a slope of − 14 HB/wt% Fe at this concentration range is notably smaller than the global regression slope of − 32.5 HB/wt% (Table 3), confirming the threshold behavior of Fe: at the low concentrations present in 7075 (0.25 wt%), Fe-based intermetallic formation is already limited, and full elimination provides only moderate gain (Karabulut et al., 2024; Sankanit et al., 2022). The larger linear regression slope reflects the steeper penalty imposed by higher Fe concentrations prevalent in less-purified alloy grades (Hahn & Rosenfield, 1975; Kobayashi, 2000).

The Pareto-optimal composition (Var. 14: Cu = 2.20, Mg = 2.90, Zn = 7.10, Fe = 0.00 wt%) combines elevated Zn and Mg for maximized $MgZn_2$ and S-phase (Al_2CuMg) precipitation (Lee et al., 2016; N. Ma et al., 2024; Salleh et al., 2022), increased Cu to promote S-phase volume fraction, and complete Fe elimination to remove damage nucleation sites (W. Dai et al., 2022; Mukherjee et al., 2023). This composition yields predicted HB = 179.6 and UTS = 599.3 MPa, representing concurrent improvements of 19.7% and 9.3% over the AA 7075-T6 baseline. The predicted UTS/HB of 3.34 satisfies the Tabor feasibility bounds, and the Pareto contour in Fig. 6a positions this composition in the high-Zn, high-Mg quadrant where both UTS (color map) and HB (isolines) are simultaneously maximized.

Table 3
Predicted HB and UTS for 12 AA 7075-T6 composition variants by PI-MLDS. ΔUTS/HB column reports the predicted Tabor ratio for each variant. Bold row = Pareto-optimal composition (Var. 14).

Variant	Cu (wt%)	Mg (wt%)	Zn (wt%)	Fe (wt%)	HB Predicted	UTS Predicted (MPa)	ΔHTS/HB
Exp. (7075-T6 baseline)	1.60	2.50	5.60	0.25	150.0	548.4	3.66
Var. 1 – Zn + 0.5 wt%	1.60	2.50	6.10	0.25	150.1	559.6	3.73
Var. 2 – Zn + 1.5 wt%	1.60	2.50	7.10	0.25	154.3	575.9	3.73
Var. 3 – Cu + 0.4 wt%	2.00	2.50	5.60	0.25	149.9	558.6	3.73
Var. 4 – Mg + 0.3, Zn + 1.0 wt%	1.60	2.80	6.60	0.25	156.2	571.0	3.66
Var. 5 – Mg − 0.5 wt%	1.60	2.00	5.60	0.25	142.3	541.6	3.81
Var. 6 – Cu + 0.9, Mg + 0.3, Zn + 0.9	2.50	2.80	6.50	0.25	155.8	586.8	3.77
Var. 7 – Mg + 0.5 wt%	1.60	3.00	5.60	0.25	156.1	552.6	3.54
Var. 8 – Fe → 0.00 wt%	1.60	2.50	5.60	0.00	153.5	561.6	3.66
Var. 9 – Cu − 0.4 wt%	1.20	2.50	5.60	0.25	149.6	536.5	3.59
Var. 10 – Ti − 0.05 wt%	1.60	2.50	5.60	0.25	142.9	524.2	3.67
Var. 14 – Pareto optimal	**2.20**	**2.90**	**7.10**	**0.00**	**179.6**	**599.3**	**3.34**

Note: All variants use T6 temper encoding. Remaining elements held at AA 7075-T6 baseline values (Si = 0.40, Mn = 0.30, Cr = 0.23, Ti = 0.06, Zr = 0.00 wt%). SVR used for UTS prediction; GBR for HB prediction.

3.6. Compositional Effect Analysis: PCC, Sensitivity, and Feature Importance

Table 4 and Figs. 7–8 present the three-metric compositional analysis. Three elements Zn, Cu, and Mg show statistically significant positive relationships with both targets at $p < 0.001$. Fe shows significant negative relationships (HB: $p = 0.042$; UTS: $p = 0.007$). The remaining five elements (Si, Mn, Cr, Ti, Zr) show non-significant linear correlations, though their contributions appear through nonlinear effects captured by GBR importance scores.

Table 4
Tri-metric compositional analysis: Pearson correlation coefficients (PCC), linear regression sensitivity slopes with significance levels, and GBR feature importance (FI) scores for Brinell hardness and UTS. Significance: *** p < 0.001, ** p < 0.01, * p < 0.05, ns = not significant.

Element	PCC – HB	Slope HB (HB/wt%)	p-value HB	PCC – UTS	Slope UTS (MPa/wt%)	p-value UTS	FI – HB	FI – UTS	FI Rank
Zn	+ 0.587	+ 11.5	< 0.001***	+ 0.593	+ 43.3	< 0.001***	0.053	0.067	4
Cu	+ 0.442	+ 10.9	< 0.001***	+ 0.485	+ 44.6	< 0.001***	0.430	0.463	1
Mg	+ 0.344	+ 7.2	< 0.001***	+ 0.386	+ 32.2	< 0.001***	0.204	0.224	2
Cr	+ 0.096	+ 49.3	0.280 ns	+ 0.113	+ 215.1	0.203 ns	0.009	0.002	9
Ti	+ 0.012	+ 11.8	0.899 ns	−0.010	−38.0	0.913 ns	0.015	0.004	8
Mn	+ 0.028	+ 3.4	0.731 ns	+ 0.049	+ 22.6	0.538 ns	0.005	0.004	10
Fe	−0.159	−32.5	0.042*	−0.212	−161.5	0.007**	0.027	0.026	6
Si	−0.013	−0.4	0.867 ns	−0.052	−6.2	0.508 ns	0.022	0.014	7
Zr	−0.772†	−1306	0.001***	−0.748	−4710	0.001***	0.002	0.001	11

Note: PCC and slopes computed on alloys with non-zero element concentrations. FI = GBR mean decrease in impurity, summing to 1.00 per target (heat treatment indicators account for the remaining importance not shown).

The PCC ranking for both targets places Zn first (HB: +0.587; UTS: +0.593) with the highest correlation magnitude, followed by Cu (+ 0.442; +0.485) and Mg (+ 0.344; +0.386). However, GBR feature importance produces a strikingly different ranking: Cu dominates for both HB (0.430) and UTS (0.463), exceeding Mg (0.204; 0.224) and Zn (0.053; 0.067) by large margins. This PCC-importance divergence reveals a

fundamental distinction: Zn is a powerful linear discriminator across the dataset because it perfectly separates 7xxx alloys (Zn > 4 wt%, high HB and UTS) from all other series (Zn < 2 wt%, lower properties), producing high global correlation. Cu, by contrast, spans a bimodal range high in 2xxx alloys (Cu: 2–6 wt%) and low in 5xxx/6xxx/1xxx alloys (Cu < 0.5 wt%) generating complex nonlinear composition-property relationships that GBR tree splits resolve more effectively than linear PCC. The element sensitivity regression confirms this: Cu yields a significant slope of + 10.9 HB/wt% ($p < 0.001$), nearly matching Zn (+ 11.5 HB/wt%, $p < 0.001$), yet Cu has lower PCC owing to its non-monotonic relationship with hardness across series boundaries.

The heat treatment indicator for the O (annealed) temper ranks third in GBR importance for both HB (0.134) and UTS (0.130), reflecting the dominant property-determining role of precipitation state independent of composition: annealed alloys in the dataset show mean HB = 50 ± 15 and UTS = 194 ± 58 MPa versus T6-aged alloys at 124 ± 33 HB and 442 ± 143 MPa a factor-of-two property increase attributable entirely to precipitation hardening. This finding underscores that alloy temper information is non-optional for accurate ML property prediction: models trained without temper encoding would inherit systematic errors equivalent to the T6-O property gap across the dataset.

The Zr row in Table 4 requires particular care in interpretation. The extreme sensitivity slopes (-1306 HB/wt%; -4710 MPa/wt%) and high PCC magnitudes (r = -0.772; -0.748) arise from only 32 non-zero Zr data points, all derived from advanced alloys where Zr additions (0.10–0.175 wt%) co-occur with other premium microalloying elements. The apparent negative correlation is a confounding artifact: high-Zr alloys in this dataset tend to be overaged T7-temper variants with lower HB and UTS than peak-aged equivalents. The GBR importance of Zr is negligible (0.002; 0.001) because the model correctly identifies Zr's limited predictive contribution once temper class and other elements are accounted for. This divergence between high linear PCC and low nonlinear importance provides a cautionary example for compositional effect analysis in sparse datasets.

4. Discussion

4.1. SVR Superiority and Algorithm Selection Principles for Multi-Series Datasets

The uniform superiority of SVR with RBF kernel across both HB and UTS targets in this multi-series dataset contradicts the common expectation derived from single-series, single-target aluminum alloy ML studies that ensemble tree methods dominate for small to medium materials databases. The key factor is dataset heterogeneity: when training data spans seven alloy series with fundamentally different strengthening mechanisms (pure solid solution in 1xxx, precipitation hardening in 2xxx and 7xxx, work hardening in 5xxx), the property-composition response surface exhibits distinct subspace geometries separated by sharp series boundaries. SVR with RBF kernel maps the compositional space to a high-dimensional kernel feature space where these boundaries become separating hyperplanes, enabling smooth global interpolation within each subspace. GBR, while effective for single-series or single-mechanism datasets, generates discontinuous boundaries at tree splits that can introduce artifacts near series boundaries explaining its slightly lower R^2 despite having more hyperparameters and greater modeling flexibility.

ANN's underperformance for HB prediction (R^2 = 70.0%) despite comparable UTS accuracy (87.9%) reveals an important target-specific limitation. Brinell hardness is inherently more sensitive to local microstructural heterogeneity precipitate coherency state, grain boundary precipitate-free zone width, and sub-grain dislocation density that are not captured by bulk composition and temper class inputs. This introduces irreducible prediction noise that ANN, with its high-dimensional weight space, amplifies through overfitting to training-set patterns. UTS, integrating over larger deformation volumes, exhibits lower sensitivity to this local microstructural scatter, enabling ANN to generalize better. KNN's consistent underperformance reflects its fundamental limitation in high-dimensional composition spaces: with 18 features (9 elements + 9 temper indicators), the Euclidean distance metric fails to discriminate compositionally distant alloys with similar single-element concentrations, degrading the quality of the k-nearest neighborhood for prediction.

The practical design implication is that for multi-series aluminum alloy databases, SVR with RBF kernel should be the default algorithm choice for both hardness and tensile strength prediction, while GBR provides competitive accuracy with greater interpretability through tree structure and native feature importance computation. ANN should be reserved for situations where dataset size exceeds 500 + points, where its global function approximation capability can stabilize convergence. KNN, while computationally simple, is not recommended for datasets spanning multiple alloy families with compositionally distinct strengthening mechanisms.

4.2. Mechanistic Interpretation of Composition-Property Relationships

The tri-metric analysis in Table 3 and Figs. 7–8 enables mechanistic decomposition of how individual alloying elements control hardness and tensile strength through distinct linear and nonlinear pathways. Zinc's position as the highest-PCC element (r = 0.587 for HB, 0.593 for UTS) reflects its role as the compositional marker separating high-strength 7xxx alloys from all other series in the dataset a linear discriminative

function rather than a causal strengthening mechanism for alloys within a single series. Within the 7xxx series itself, Zn strengthens through $MgZn_2$ (η'/η phase) precipitation (Sun et al., 2025; Tan et al., 2022), where the critical volume fraction scales with Zn content (Y. Dai et al., 2022; Fang et al., 2014). The sensitivity slope of + 11.5 HB/wt% Zn and + 43.3 MPa/wt% Zn (Table 3) integrates this within-7xxx effect with the cross-series discriminative effect. The composition variant analysis confirms a super-linear Zn effect at elevated concentrations: a 1.5 wt% Zn increase (Var. 2) raises HB by 4.3 and UTS by 27.5 MPa, exceeding three times the response expected from linear scaling of the + 0.5 wt% increment in Var. 1.

Copper's dominance in GBR feature importance (0.430 for HB, 0.463 for UTS) despite lower PCC than Zn reflects its structurally complex, series-spanning role. In 2xxx alloys, Cu is the primary strengthening element through θ' (Al_2Cu) and S-phase (Al_2CuMg) precipitation (Li et al., 2024; Rasouli et al., 2022), contributing the highest property levels in the dataset (2xxx mean: 95 HB, 357 MPa UTS). In 5xxx and 6xxx alloys, Cu is present only as an impurity below 0.5 wt%, contributing minimally. This bimodal compositional role means that Cu content effectively discriminates 2xxx alloys from all others but through a different mechanism than Zn's 7xxx discrimination. GBR captures this by placing an early tree split at Cu ≈ 1.0 wt%, efficiently separating 2xxx high-Cu behavior from all other alloys. The sensitivity slope of + 10.9 HB/wt% Cu and + 44.6 MPa/wt% Cu is statistically equivalent to Zn's slopes, consistent with both elements generating similar strengthening increments per weight percent through their respective precipitation sequences.

Magnesium's consistent positive effect across both targets (slope: +7.2 HB/wt%, r = 0.344; +32.2 MPa/wt%, r = 0.386, both $p < 0.001$) reflects its multi-mechanism role: solid solution strengthening through stacking fault energy reduction in 5xxx alloys (Lee et al., 2016), $MgZn_2$ and S-phase precipitation in 7xxx alloys (Fang et al., 2014b), and β" Mg_2Si precipitation in 6xxx alloys. This mechanistic diversity across series explains Mg's intermediate GBR importance (0.204 for HB): unlike Cu and Zn that discriminate specific high-strength series, Mg provides moderate strengthening across all series, producing a broad but less discriminative compositional signature. The composition variant analysis quantifies the Mg-HB coupling: +0.5 wt% Mg (Var. 7) raises HB by 6.1 (+ 4.1%) while raising UTS by only 4.2 MPa (+ 0.8%), confirming that at elevated Mg concentrations, hardness responds more sensitively than tensile strength consistent with Mg's role in increasing precipitate number density (which raises contact hardness through dislocation pinning) more than precipitate volume fraction (which would equally benefit both properties through Orowan strengthening).

Iron exhibits the only statistically significant negative relationship with both targets (HB: slope − 32.5 HB/wt%, r = -0.159, p = 0.042; UTS: slope − 161.5 MPa/wt%, r = -0.212, p = 0.007). The steeper UTS sensitivity (-161.5 MPa/wt% Fe versus − 32.5 HB/wt%) is mechanistically significant: coarse needle-like Al_3Fe and Al(FeMn)Si intermetallic particles which form above 0.3–0.5 wt% Fe during casting and solidification preferentially reduce UTS through accelerated crack initiation under tensile loading, while their effect on localized hardness which is dominated by matrix properties is comparatively smaller (Yi et al., 2022). The composition variant analysis confirms a moderate Fe benefit at the 7075-baseline concentration (0.25 wt%): full Fe elimination (Var. 8) raises HB by 3.5 (+ 2.3%) and UTS by 13.2 MPa (+ 2.4%). The smaller-than-expected benefit (global slope suggests − 32.5 × 0.25 = -8.1 HB penalty for 0.25 wt% Fe) reflects the threshold behavior at 0.25 wt% Fe, intermetallic formation is limited, and the benefit of elimination is smaller than at higher Fe concentrations prevalent in lower-purity alloy grades. This threshold mechanism, which the GBR model captures through a specific tree split near Fe ≈ 0.3 wt%, explains why Fe ranks sixth in feature importance despite being the sole statistically significant negative linear predictor.

4.3. Pareto Optimization: Design Strategy and Practical Implications

The Pareto-optimal composition (Var. 14: Cu = 2.20, Mg = 2.90, Zn = 7.10, Fe = 0.00 wt%) achieves predicted HB = 179.6 and UTS = 599.3 MPa through the cooperative action of three distinct mechanisms. First, elevated Zn (7.10 wt%) drives $MgZn_2$ precipitation beyond the critical volume fraction for peak hardening, consistent with the super-linear Zn response observed in Var. 1 versus Var. 2. Second, elevated Mg (2.90 wt%) simultaneously increases the $MgZn_2$ precipitate number density and contributes S-phase (Al_2CuMg) precipitation through interaction with the elevated Cu content (2.20 wt%), broadening the precipitation hardening contribution (Fang et al., 2014b; Tao et al., 2026). Third, complete Fe elimination removes grain boundary intermetallic particles that would otherwise serve as fatigue and tensile crack initiation sites.The predicted UTS/HB ratio of 3.34 for Var. 14 falls within the T6 temper-class mean range (3.49–3.51), confirming compositional and thermal processing consistency.

The predicted properties of Var. 14 position this composition within the performance envelope of commercial premium-grade 7xxx variants. AA 7068-T6511 reports UTS of 641–683 MPa and HB of approximately 170–196 (Tao et al., 2026), while AA 7085-T7651 exhibits UTS of 490–537 MPa and HB of 143–162. The Pareto optimal Var. 14 prediction of HB = 179.6 and UTS = 599.3 MPa lies between these benchmarks, suggesting that this composition if experimentally synthesized would produce properties competitive with the higher-strength side of the 7xxx commercial portfolio. The Zn content of 7.10 wt% remains below the threshold (approximately 8.0 wt%) above which non-equilibrium T-phase (AlZnMgCu) coarsening begins to reduce fracture toughness (Cai et al., 2023), indicating that the predicted composition does not sacrifice toughness for strength at the predicted Zn level.

4.4. Limitations and Recommendations for Future Work

Three primary limitations constrain the current PI-MLDS. First, the 163-point dataset size produces high k-fold standard deviations (0.176–0.237) and LOO MAPE values exceeding 20% for HB in the 6xxx series. Expanding the dataset particularly for 6xxx, 3xxx, and 8xxx (Al-Li) alloys under diverse temper conditions is the highest priority for improving prediction reliability. Second, the absence of microstructural descriptors (grain size, precipitate volume fraction, coherency strain, dislocation density) as input features imposes a fundamental accuracy ceiling: composition and temper class alone cannot fully predict HB, which is critically sensitive to local precipitate state. Future integration of microstructural data from TEM, SAXS, or coupled thermodynamic simulation would enable process-structure-property linkage beyond composition-property modeling. Third, the Tabor constraint, while effective as an inverse design feasibility filter, would be more powerful if embedded directly within the model training objective through a multi-output loss function, which SVR and GBR do not natively support. Extension to neural network architectures with custom multi-objective loss functions incorporating the Tabor constraint as a weighted physics penalty represents a natural progression of this work.

5. Conclusions

A physics-informed machine learning design system (PI-MLDS) was developed, benchmarked, and validated for dual-target prediction and Pareto optimization of Brinell hardness and UTS across 163 multi-element aluminum alloys spanning the 1000–7000 series. The following conclusions are supported by experimental data. SVR with RBF kernel outperforms all competing algorithms for both targets simultaneously, achieving R^2 = 86.3% (HB) and 89.3% (UTS) on the hold-out test set with the smallest k-fold standard deviation for UTS (0.176), establishing SVR as the recommended algorithm for multi-series aluminum alloy databases where compositional heterogeneity and series boundary effects dominate the prediction landscape. ANN achieves comparable UTS accuracy to SVR and GBR (R^2 = 87.9%) but substantially underperforms for HB (R^2 = 70.0%), revealing a target-specific limitation: HB is more sensitive to local microstructural heterogeneity not captured by composition-temper inputs, and ANN amplifies this noise through overfitting at the 163-point data scale. The PI-MLDS Tabor constraint (UTS/HB empirical mean = 3.712, bounds [2.0, 6.0]) validates all test-set dual-output predictions as physically consistent, while also revealing systematic temper-class dependence of the UTS/HB ratio: T3 and O-temper alloys exhibit the highest ratios (3.94; 3.89) and peak-aged T6/T8 alloys the lowest (3.49–3.51), providing mechanistically interpretable guidance for alloy design. Leave-one-out PI-MLDS validation across six reference alloys yields mean MAPE of 12.7% (HB) and 6.5% (UTS), with the 7050-T7451 alloy achieving the best prediction accuracy (HB: 0.4%, UTS: 1.6%) and 6061-T6/T651 the worst HB accuracy (27.0%) owing to sparse 6xxx training coverage. Tri-metric compositional analysis reveals a mechanistically important divergence between linear (PCC) and nonlinear (GBR importance) rankings: Zn dominates PCC (r = 0.587, 0.593) through cross-series linear discrimination, while Cu dominates GBR importance (0.430, 0.463) through its complex bimodal composition range spanning 2xxx (high-Cu) and all other series (low-Cu). Fe is the sole statistically significant negative predictor for both targets (HB: p = 0.042; UTS: p = 0.007), acting through a concentration-threshold intermetallic embrittlement mechanism that GBR resolves through a tree split near Fe ≈ 0.3 wt%. Multi-objective Pareto optimization identifies a 7075-based composition (Cu = 2.20, Mg = 2.90, Zn = 7.10, Fe = 0.00 wt%, T6) with predicted HB = 179.6 and UTS = 599.3 MPa concurrent improvements of 19.7% and 9.3% over AA 7075-T6 at a Tabor-consistent UTS/HB ratio of 3.34, positioning this composition within the performance envelope of commercial high-strength 7xxx premium variants.

Declarations

Declaration of generative ai and AI-assisted technologies in the writing process

During the preparation of this work, the authors used Gemini to refine the spelling and wording of the paragraph. After using this tool/service, the authors reviewed and edited the content as needed and take full responsibility for the content of the publication.

CRediT Authorship Contribution Statement

Deni Haryadi: Writing – original draft, Visualization, Investigation. **Aji Abdillah Kharisma**: Supervision, Software. **Yudan Whulanza**: Methodology, Funding acquisition. **Imam Sofii**: Formal analysis. **Mahfud Ibadi**: Resources, Methodology. **Yunus Bakhtiar Arafat**: Validation, Conceptualization. **Haris Rudianto**: Writing – review & editing, Project administration, Data curation

Declaration of Competing Interest

The authors declare no known competing financial interests or personal relationships that could have influenced the work reported in this paper.

Data Availability

Data will be made available on request.

References

1. Al Bhadle BMA, Hassoni SM, Hassan KS (2024) IMPROVEMENT FRICTION WELDED 6063 – T6 ALUMINUM ALLOY JOINT PROPERTIES. Int J Appl Mech Eng 29(4). https://doi.org/10.59441/ijame/192271
2. Azimi H, Bonakdari H, Ebtehaj I (2019) Design of radial basis function-based support vector regression in predicting the discharge coefficient of a side weir in a trapezoidal channel. Appl Water Sci 9(4). https://doi.org/10.1007/s13201-019-0961-5
3. Cai Q, Liu B, Chen X, Xi W, Cheng J (2023) Effect of Sb Modification and B Refinement on the Microstructure and Properties of as-Cast Al–7Si–0.35Mg Alloy. Int J Metalcast 17(2). https://doi.org/10.1007/s40962-022-00830-9
4. Dai W, Zhang C, Zhao L, Li C (2022) Effects of Cu content in Al-Cu alloys on microstructure, adhesive strength, and corrosion resistance of thick micro-arc oxidation coatings. *Materials Today Communications*, *33*. https://doi.org/10.1016/j.mtcomm.2022.104195
5. Dai Y, Yan L, Hao J (2022) Review on Micro-Alloying and Preparation Method of 7xxx Series Aluminum Alloys: Progresses and Prospects. In *Materials* (Vol. 15, Number 3). https://doi.org/10.3390/ma15031216
6. Diniz SB, dos Santos Paula A, Brandão LPM (2023) Structural Characterization of the Rolled and Annealed 7475 Aluminum Alloy. J Mater Eng Perform 32(2). https://doi.org/10.1007/s11665-022-07120-9
7. Elamin NY, Elamin MR, Alhussain H, Elshaarawy RFM, Habba MIA, Fouad RA (2025) Influence of Cu and Ni addition on metallurgical, mechanical, and corrosion behavior of TIG welded Al-Mg-Si alloy. *International Journal of Pressure Vessels and Piping*, *216*. https://doi.org/10.1016/j.ijpvp.2025.105533
8. Fang HC, Chao H, Chen KH (2014a) Effect of Zr, Er and Cr additions on microstructures and properties of Al-Zn-Mg-Cu alloys. *Materials Science and Engineering: A*, *610*. https://doi.org/10.1016/j.msea.2014.05.021
9. Fang HC, Chao H, Chen KH (2014b) Effect of Zr, Er and Cr additions on microstructures and properties of Al-Zn-Mg-Cu alloys. Mater Sci Engineering: A 610:10–16. https://doi.org/10.1016/j.msea.2014.05.021
10. Farahany S, Timelli G (2025) Effect of cadmium and strontium/cadmium ratio on the microstructure, solidification characteristics, and mechanical properties of Al-7Si-0.4Mg cast alloy. *Journal of Alloys and Compounds*, *1045*. https://doi.org/10.1016/j.jallcom.2025.184788
11. Fatriansyah JF, Satrio MRR, Federico A, Suhariadi I, Dhaneswara D, Gascoin N (2024) Machine learning-based forward and inverse designs for prediction and optimization of fracture toughness of aluminum alloy. *Results in Engineering*, *23*. https://doi.org/10.1016/j.rineng.2024.102717
12. Hahn GT, Rosenfield AR (1975) Metallurgical factors affecting fracture toughness of aluminum alloys. Metall Trans A 6(3). https://doi.org/10.1007/BF02672285
13. Hao J, Yan L, Dai Y (2023) Effect of rare earth Nd on the microstructural transformation and mechanical properties of 7xxx series aluminum alloys. Reviews Adv Mater Sci 62(1). https://doi.org/10.1515/rams-2023-0345
14. Haque MS, Moeed KM (2025) Exploring the Influence of CMT Welding Parameters on the Microstructure and Mechanical Properties of Dissimilar AA6082-T6 and AA7075-T6 Joints. J Adv Manuf Syst. https://doi.org/10.1142/S0219686726500319
15. Harti JI, Prasad TB, Nagaral M, Jadhav P, Auradi V, Prakash SS (2021) Microstructure, Mechanical Behavior and Tensile Fractography of 90-Micron-Sized Titanium Carbide Particles Reinforced Al2219 Alloy Die Cast Metal Composites. J Fail Anal Prev 21(2). https://doi.org/10.1007/s11668-020-01107-1
16. Hu X, Luo Z, Liu S, Ren Y, Long W (2025) Effect of Stirring Needle Length on the Microstructures and Properties of A380/6061 Dissimilar Aluminium Alloy FSW Joints. Materials 18(7). https://doi.org/10.3390/ma18071621
17. Jain S, Mishra RS (2022) Effect of Al2O3 nanoparticles on microstructure and mechanical properties of friction stir-welded dissimilar aluminum alloys AA7075-T6 and AA6061-T6. *Proceedings of the Institution of Mechanical Engineers, Part E: Journal of Process Mechanical Engineering*, *236*(4). https://doi.org/10.1177/09544089211065534
18. Jiang J, Jiang F, Zhang M, Tang Z, Tong M (2021) The recrystallization behavior of shear band in room temperature ECAPed Al-Mg-Mn-Sc-Zr alloy. *Materials Characterization*, *175*. https://doi.org/10.1016/j.matchar.2021.111081
19. Karabulut C, Malkoç G, Kaya AY, Özaydin O, Yayla P (2024) Influence of Different Fe Levels on Mechanical Properties of AlSi7Mg0.3 Aluminum Casting Alloys. Int J Metalcast 18(4). https://doi.org/10.1007/s40962-023-01227-y
20. Kobayashi T (2000) Strength and fracture of aluminum alloys. Mater Sci Engineering: A 280(1):8–16. https://doi.org/10.1016/S0921-5093(99)00649-8
21. Kong J, An L, Zheng J, Du X (2025) Effect of Zn Addition on Microstructure and Mechanical Properties of a Hypoeutectic Al–7Si-Based Alloy. Int J Metalcast. https://doi.org/10.1007/s40962-025-01594-8
22. Lee BH, Kim SH, Park JH, Kim HW, Lee JC (2016) Role of Mg in simultaneously improving the strength and ductility of Al-Mg alloys. *Materials Science and Engineering: A*, *657*. https://doi.org/10.1016/j.msea.2016.01.089

23. Li C, Zhang H, Guo D, Zeng W (2024) Crystal Structure Prediction and Property Calculation of Al2CuMg by Deep Learning Potential. J Mater Eng Perform 33(24). https://doi.org/10.1007/s11665-023-08944-9
24. Ma K, Hu T, Yang H, Topping T, Yousefiani A, Lavernia EJ, Schoenung JM (2016) Coupling of dislocations and precipitates: Impact on the mechanical behavior of ultrafine grained Al-Zn-Mg alloys. *Acta Materialia*, *103*. https://doi.org/10.1016/j.actamat.2015.09.017
25. Ma N, Zhu J, Chang K, Qin Y (2024) Effect of Mg on Plasticity and Microstructure of Al-Mg-Ga-Sn-In Soluble Aluminum Alloy. Materials 17(21). https://doi.org/10.3390/ma17215287
26. Mamun O, Bause M, Ebna Hai BSM (2025) Accelerated development of multi-component alloys in discrete design space using Bayesian multi-objective optimisation. Mach Learning: Sci Technol 6(1). https://doi.org/10.1088/2632-2153/ada47d
27. Masood Chaudry U, Hamad K, Abuhmed T (2021) Machine learning-aided design of aluminum alloys with high performance. *Materials Today Communications*, *26*. https://doi.org/10.1016/j.mtcomm.2020.101897
28. Moustafa EB, Natto HD, Banoqitah EM, Alazwari MA, Mosleh AO, Khalil AM (2025) Improving the mechanical and dynamic properties of Al-Zn-Mg-Cu- based aluminum alloy: A combined approach of microstructural modification and heat treatment. *Journal of Alloys and Compounds*, *1013*. https://doi.org/10.1016/j.jallcom.2025.178558
29. Mukherjee D, Mukherjee M, Mandal N, Samanta SK, Maiti A (2023) Effect of micro-alloying on the characteristics of as-cast Al-Zn-Cu-Mg-X alloy with varying Cu and Zn. *Materials Today Communications*, *34*. https://doi.org/10.1016/j.mtcomm.2023.105445
30. Nariman-zadeh N, Darvizeh A, Jamali A (2006) Pareto optimization of energy absorption of square aluminium columns using multi-objective genetic algorithms. *Proceedings of the Institution of Mechanical Engineers, Part B: Journal of Engineering Manufacture*, *220*(2). https://doi.org/10.1243/095440506X78156
31. Natekin A, Knoll A (2013) Gradient boosting machines, a tutorial. *Frontiers in Neurorobotics*, *7*(DEC). https://doi.org/10.3389/fnbot.2013.00021
32. Patil S, Chinchanikar S (2025) Investigation on the mechanical properties of stir-cast Al7075-T6-based nanocomposites with microstructural and fractographic surface analysis. Obrabotka Metallov 27(3). https://doi.org/10.17212/1994-6309-2025-27.3-236-251
33. Rasouli M, Asgar MG, Akhlaghi F, Marjani O (2022) Preparation of Al-Al2Cu Composites In-situ Processed Via Reactive Infiltration. Metallography Microstruct Anal 11(4). https://doi.org/10.1007/s13632-022-00873-8
34. Salleh MS, Rahman AA, Abdullah RIR, Siswanto N, Subramonian S (2022) Effect of different Mg content on microstructure and mechanical properties of thixoformed Al-Si-Cu-Mg alloys. Jurnal Tribologi, *32*
35. Sankanit P, Uthaisangsuk V, Pandee P (2022) Tensile properties of hypoeutectic Al-Ni alloys: Experiments and FE simulations. *Journal of Alloys and Compounds*, *889*. https://doi.org/10.1016/j.jallcom.2021.161664
36. Settu N, Kesavan GK, Subramanian A, Ramasamy M, Rangesh A, Settu R, Mathivanan T, Praveenkumar V, Shankar KV, Manu K (2024) Optimization of tensile properties by rotary friction welded dissimilar 2014 T6 and 6082 T6 aluminium alloys. Int J Interact Des Manuf. https://doi.org/10.1007/s12008-024-01946-4
37. Song Y, Liang J, Lu J, Zhao X (2017) An efficient instance selection algorithm for k nearest neighbor regression. *Neurocomputing*, *251*. https://doi.org/10.1016/j.neucom.2017.04.018
38. Sun W, Xiang Z, Li J, Yang Z, Han Y, Chen Z (2025) Effect of TiB2 Content on Microstructure and Mechanical Properties of TiB2/Al-Zn-Mg-Cu Composites with High Zn Content. Materials 18(22). https://doi.org/10.3390/ma18225191
39. Tan P, Sui Y, Jin H, Zhu S, Jiang Y, Han L (2022) Effect of Zn content on the microstructure and mechanical properties of as-cast Al-Zn-Mg-Cu alloy with medium Zn content. *Journal of Materials Research and Technology*, *18*. https://doi.org/10.1016/j.jmrt.2022.03.168
40. Tao S, Yu M, Li Y, Wen K, Li X, Li Z, Zhang Y, Xiong B (2026) *Study on the Influence of Precipitation Characteristics on Fatigue Properties of Typical 7xxx Aluminum Alloys*. https://doi.org/10.3390/ma19081601
41. Wu DY, Hufnagel TC (2024) Efficient searching of processing parameter space to enable inverse microstructural design of materials. *Acta Materialia*, *264*. https://doi.org/10.1016/j.actamat.2023.119562
42. Xiang C, Xie L, Li J, Luo G, Fang J, Pan H (2025) Strengthening and Toughening Mechanism and Corrosion Resistance of 7003 Aluminum Alloy by Thermomechanical Treatment. J Mater Eng Perform 34(16). https://doi.org/10.1007/s11665-024-10402-z
43. Yi T, Liu S, Fang C, Jiang G (2022) Eliminating hole defects and improving microstructure and mechanical properties of friction stir welded joint of 2519 aluminum alloy via TIG arc. J Mater Process Technol 310. https://doi.org/10.1016/j.jmatprotec.2022.117773
44. Zang R, Ding L, Ehlers FJH, Jia Z, Xu S, Li Y, Cao L (2023) The influence of Cu content and Mg/Si ratio on the strength and formability in Al-Mg-Si-Cu alloys. *Materials Characterization*, *205*. https://doi.org/10.1016/j.matchar.2023.113355
45. Zeng C, Cai X, Qi Z, Tan Z, Wang H, Peng Y, Guo W, Qi B, Cong B (2023) Effect of in-situ synthesized TiC particles on microstructure and mechanical properties of directed energy deposited AA2219 Al-Cu alloy. *Journal of Alloys and Compounds*, *964*. https://doi.org/10.1016/j.jallcom.2023.171331

Figures

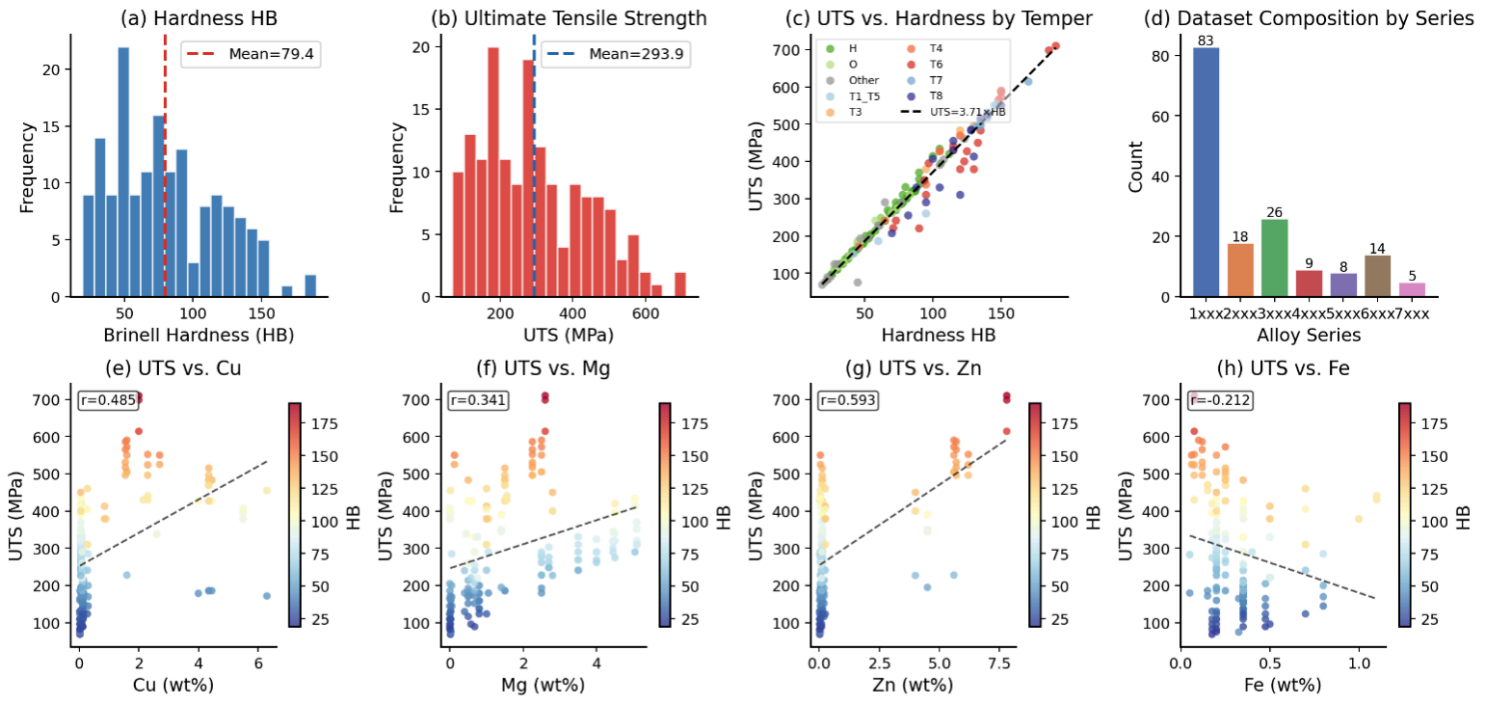

Figure 1

Dataset characterization. (a) Frequency distribution of Brinell hardness HB; (b) frequency distribution of UTS; (c) UTS versus HB scatter plot by heat treatment temper class with the empirical Tabor line (UTS = 3.71 × HB); (d) dataset composition by alloy series (count); (e–h) UTS as a function of Zn, Cu, Mg, and Fe content with linear regression overlay, Pearson r, and data points color-coded by temper group.

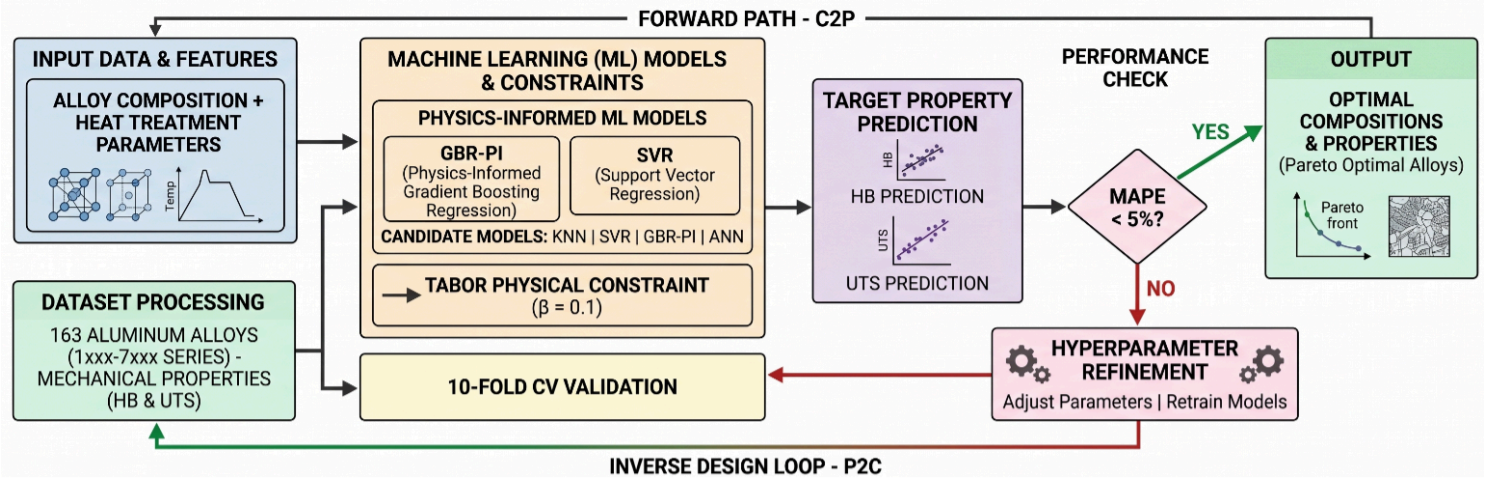

Figure 2

Physics-Informed Machine Learning Design System (PI-MLDS) workflow. The bidirectional architecture couples C2P prediction (composition HB and UTS) with P2C inverse design (target HB and UTS optimal composition). The Tabor physical constraint (UTS/HB ∈ [2.0, 6.0]) operates as a dual-stage filter: validating test-set dual-output pairs and screening P2C composition candidates. Ten-fold cross-validation provides robustness assessment at each model stage.

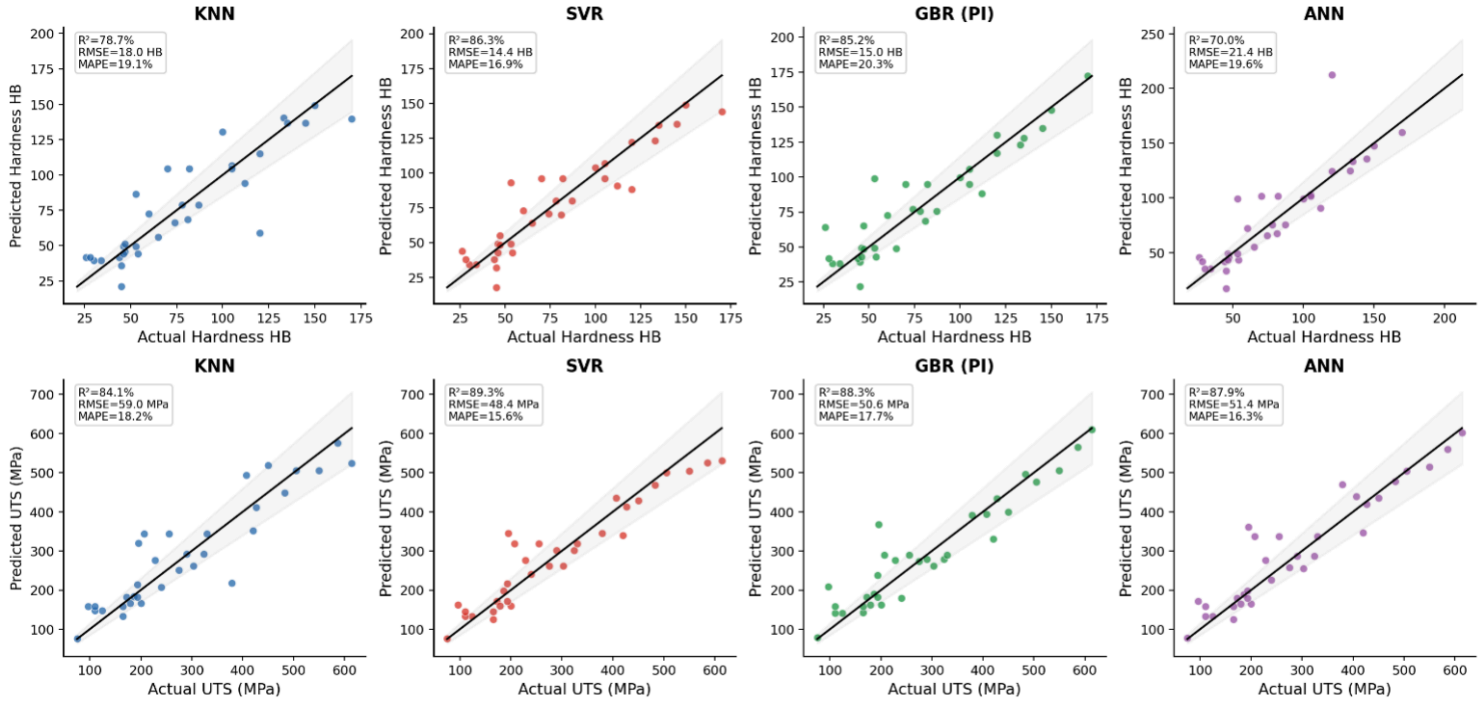

Figure 3

Actual versus predicted scatter plots for Brinell hardness HB (top row) and UTS (bottom row) across all four algorithms: (a, e) KNN; (b, f) SVR with RBF kernel; (c, g) GBR; (d, h) ANN. The solid diagonal is the ideal 1:1 line. Gray shading represents the ±15% prediction band. R², RMSE, and MAPE are annotated in each panel. Note that SVR achieves the tightest scatter around the 1:1 line for both targets.

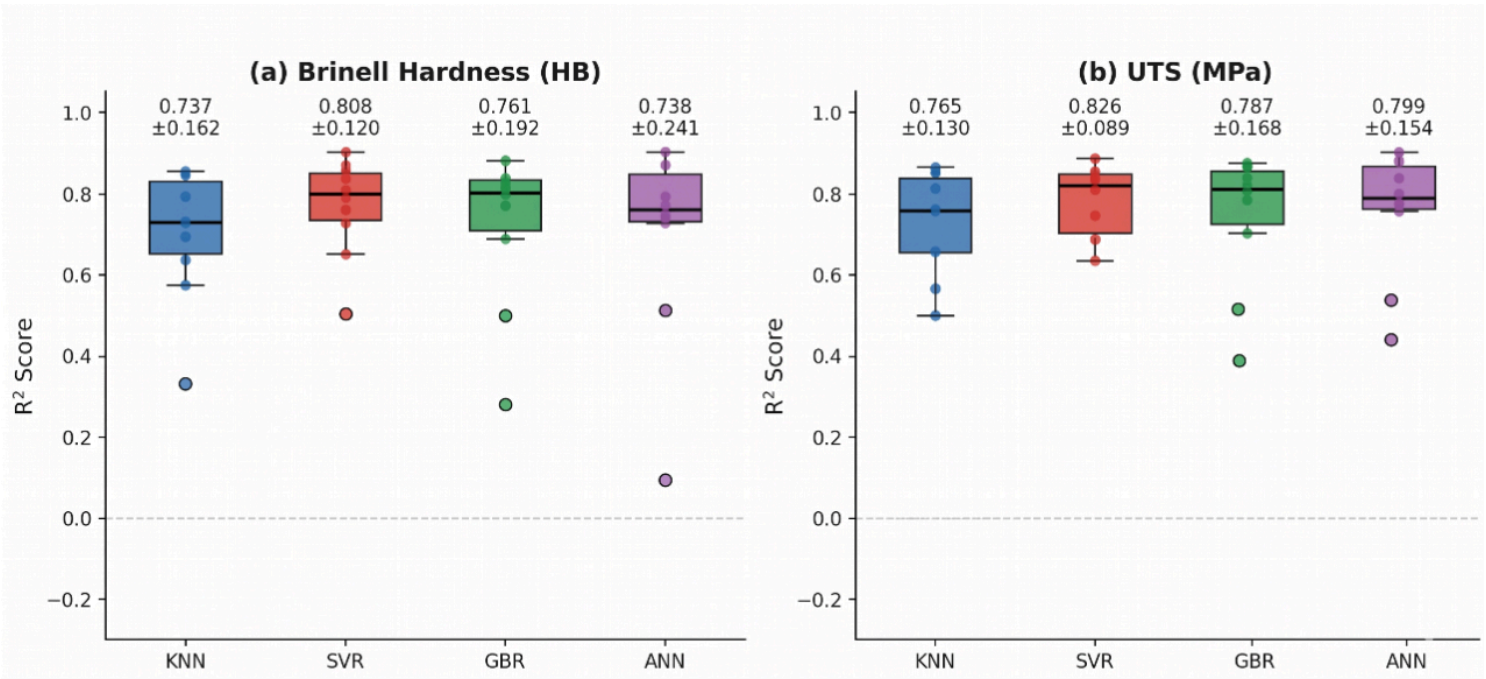

Figure 4

Ten-fold cross-validation R² score distributions for all four algorithms: (a) Brinell hardness HB; (b) UTS. Box plots show median (horizontal line), interquartile range (box), and ±1.5×IQR whiskers. Individual fold R² scores are overlaid as data points. Mean ± standard deviation is annotated above each box. SVR shows the smallest UTS standard deviation among all models.

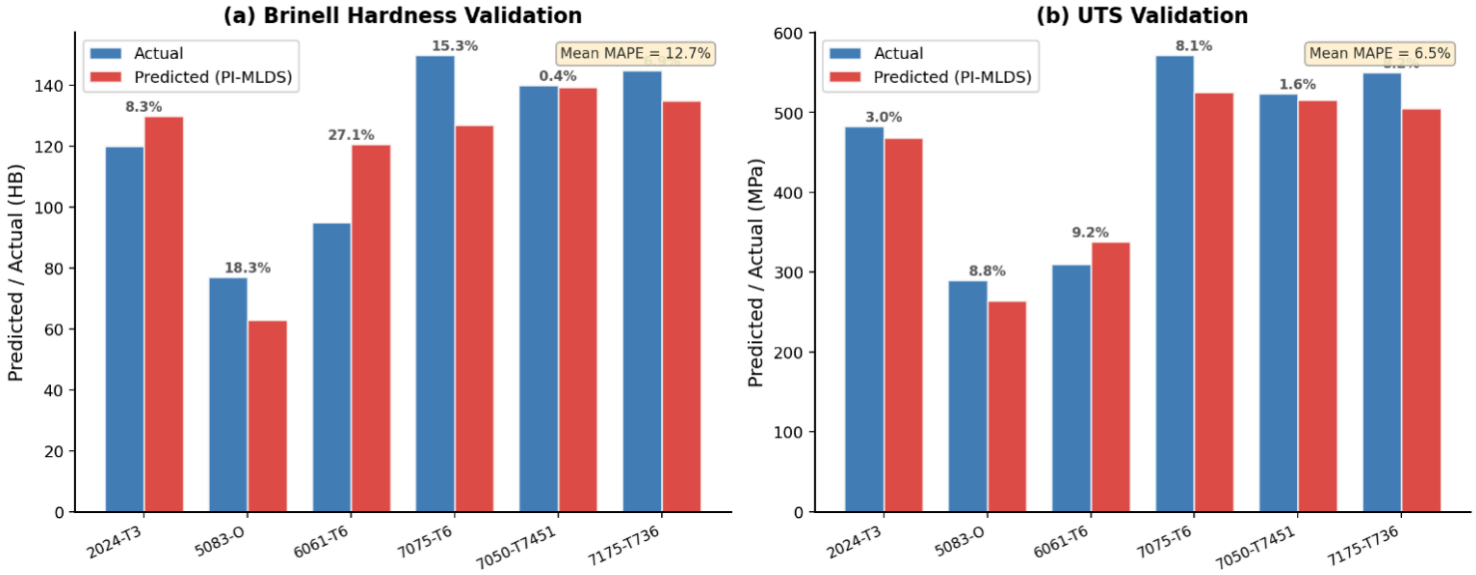

Figure 5

PI-MLDS leave-one-out validation for six commercial aluminum alloy reference cases: (a) Brinell Hardness HB; (b) UTS. Blue bars represent experimental values; red bars represent LOO-predicted values. MAPE for each alloy is annotated above the bar pairs. Overall mean MAPE is shown in the inset annotation box. UTS predictions consistently achieve lower MAPE than HB predictions across all six alloys.

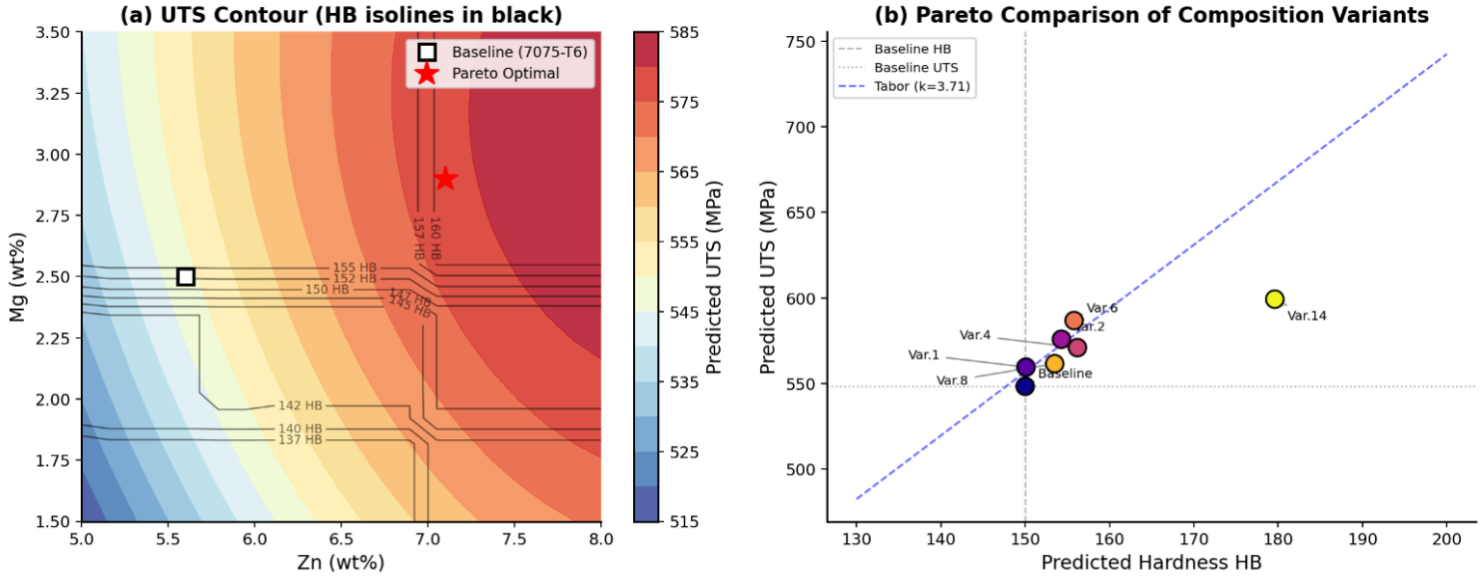

Figure 6

Multi-objective Pareto analysis. (a) Contour map of SVR-predicted UTS (color gradient) as a function of Zn content (x-axis) and Mg content (y-axis), with GBR-predicted HB isolines (dashed black lines, labeled in HB units) superimposed. Baseline AA 7075-T6 (white square) and Pareto-optimal composition Var. 14 (red star) are marked. (b) HB versus UTS scatter plot of all 12 composition variants with variant labels, baseline reference lines (dashed gray), and the empirical Tabor line (k = 3.71, blue dashed). The top-right corner defines the Pareto frontier region.

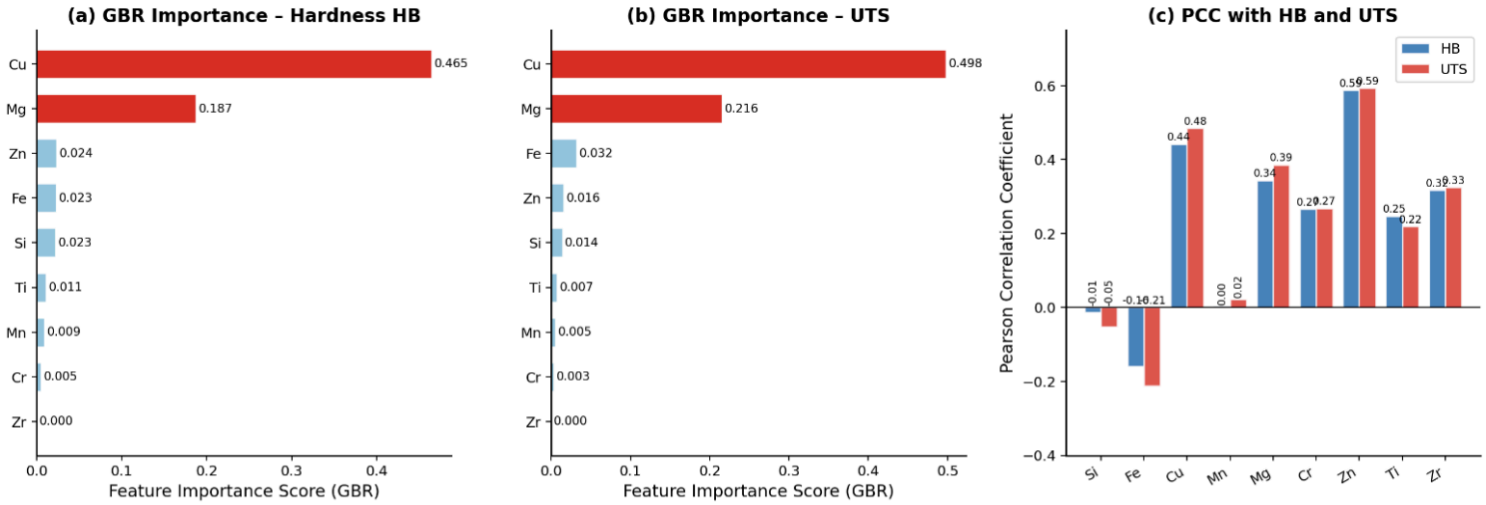

Figure 7

Compositional feature analysis. (a) GBR feature importance scores for Brinell hardness HB (ordered ascending); (b) GBR feature importance scores for UTS. (c) Pearson correlation coefficients (PCC) for all nine elemental features with HB (blue) and UTS (red), shown as a grouped bar chart. Note the marked divergence between Zn (highest PCC) and Cu (highest GBR importance), revealing distinct linear-discriminative and nonlinear-predictive roles.

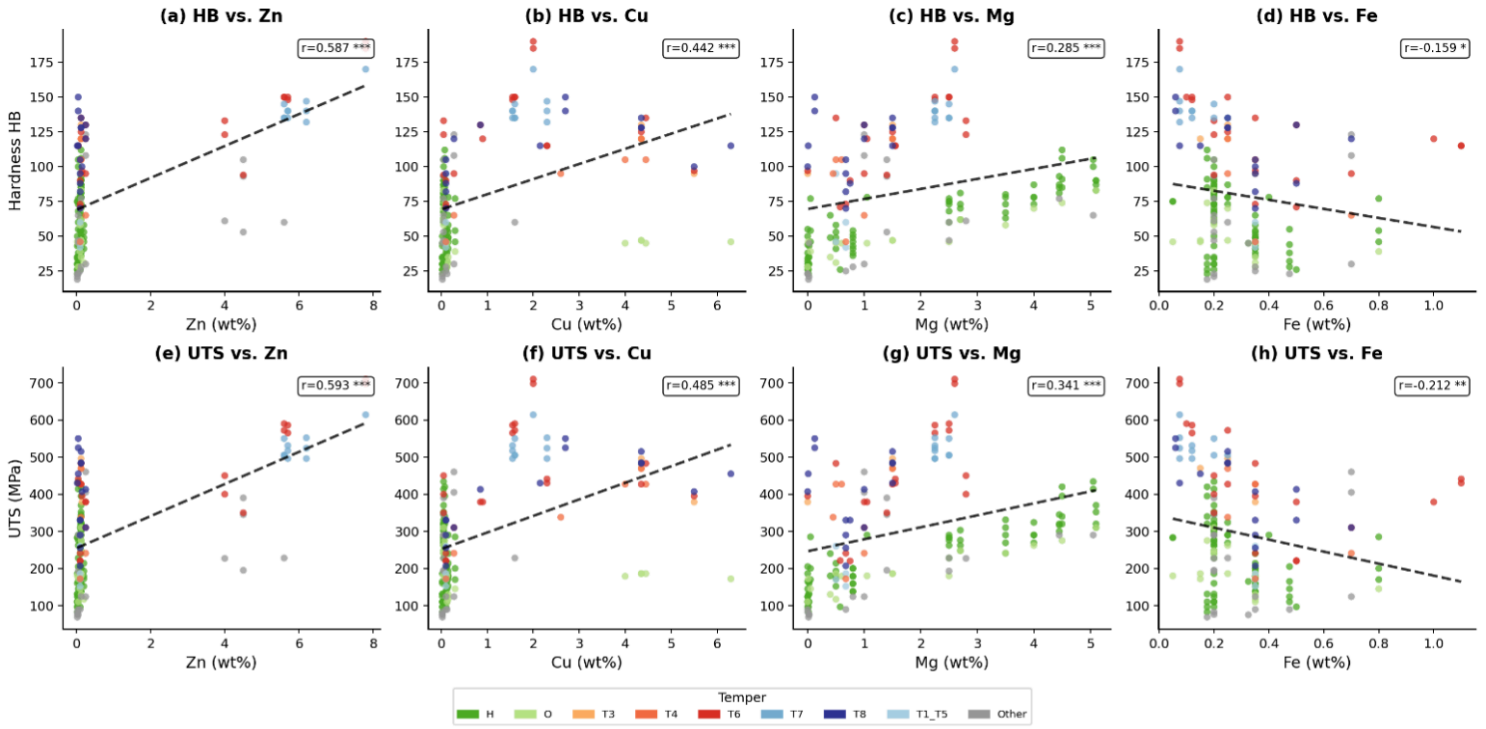

Figure 8

*Element-wise composition-property relationships for Brinell Hardness HB (top row) and UTS (bottom row): (a, e) Zn; (b, f) Cu; (c, g) Mg; (d, h) Fe. Data points are color-coded by heat treatment temper group. Black dashed lines show linear regression fits computed on non-zero elemental concentrations. Pearson r and significance level (*** p < 0.001, ** p < 0.01, * p < 0.05, ns not significant) are annotated. The spread of points at a given elemental concentration reflects the additional influence of other elements and temper class.*